



Electrochemical activity and stability of core–shell $\text{Fe}_2\text{O}_3/\text{Pt}$ nanoparticles for methanol oxidation



Yan-Ting Liu, Qin-Bo Yuan*, Dong-Hong Duan, Zhong-Lin Zhang, Xiao-Gang Hao, Guo-Qiang Wei, Shi-Bin Liu*

Chemical Engineering Department, Taiyuan University of Technology, Shanxi 030024, China

HIGHLIGHTS

- Core–shell $\text{Fe}_2\text{O}_3/\text{Pt}$ nanoparticles with amorphous iron oxide cores are synthesized.
- The influences of the amorphous iron oxide cores on Pt shells are discussed.
- The catalytic properties of the nanoparticles for methanol oxidation are studied.
- The catalytic properties of Pt shell can be tuned by varying its surface coverage.

ARTICLE INFO

Article history:

Received 21 March 2013

Received in revised form

22 May 2013

Accepted 5 June 2013

Available online 14 June 2013

Keywords:

Amorphous iron oxide

Platinum

Core–shell structure

Methanol oxidation reaction

Catalyst durability

Catalyst activity

ABSTRACT

Core–shell $\text{Fe}_2\text{O}_3/\text{Pt}$ nanoparticles with amorphous iron oxide cores are successfully synthesized by a two-step chemical reduction strategy. The Pt loading can be adjusted using this preparation technique to obtain a series of chemical compositions with varying amounts of Pt precursors. The morphology, structure, and composition of the as-prepared nanoparticles are characterized by transmission electron microscopy, X-ray diffraction, energy dispersive spectroscopy, and X-ray photoelectron spectroscopy. Electrocatalytic characteristics are systematically investigated by electrochemical techniques, such as cyclic voltammetry, chronoamperometry, and in situ Fourier transform infrared spectroscopy. Compared with the E-TEK 40 wt% Pt/C catalyst, the as-made $\text{Fe}_2\text{O}_3/\text{Pt}$ nanoparticles exhibit superior catalytic activity with lower peak potential and enhanced CO_2 selectivity toward methanol electrooxidation in acidic medium. The highest activity is achieved by core–shell $\text{Fe}_2\text{O}_3/\text{Pt}$ nanoparticles with a Fe/Pt atomic ratio of 2:1 (A g^{-1} of Pt) or 3:1 (mA cm^{-2}). These nanomaterials also show much higher structural stability and tolerance to the intermediates of methanol oxidation. Methanol electrooxidation reactions with higher performance can be achieved using core–shell nanoparticles with an amorphous iron oxide core and minimum Pt loading.

© 2013 The Authors. Published by Elsevier B.V. Open access under [CC BY license](http://creativecommons.org/licenses/by/3.0/).

1. Introduction

Over the past decades, fuel cells have become devices that can best meet our energy demands and create a better environment for mankind. In particular, direct methanol fuel cells (DMFCs) in portable electronic devices and transportation applications have attracted increased attention because of the much higher energy density of liquid methanol fuels than gaseous fuels, such as

hydrogen [1]. Electrocatalytic materials with high activity for the methanol oxidation reaction (MOR) are critically needed to enhance the performance of DMFCs. Currently, Pt is the most active and indispensable material for methanol oxidation, especially in acidic media. However, Pt is a precious metal and therefore very expensive. In addition, during the anodic process of methanol dehydrogenation, strongly adsorbed carbonaceous species, such as CO, are produced as reaction intermediates, heavily poisoning the Pt surface and inhibiting further adsorption of methanol molecules [2,3]. Therefore, further enhancements in Pt utilization efficiency and catalytic activity are fundamentally important for the widespread use of DMFCs [4]. Arranging Pt as thin shells on other substrates with a core–shell or decorated structure greatly enhances the utilization of Pt because of the improved dispersion of the metal. This method also improves material properties because of

* Corresponding authors. Tel.: +86 351 6111062; fax: +86 351 6018554.

E-mail addresses: sbliu@tyut.edu.cn, yqbtyut@163.com (S.-B. Liu).

the strain and ligand effects exerted by the core substrate on the supported Pt overlayer [5,6].

Metal oxides have attracted great interest for their use in catalyst supports [7], magnetic materials [8], and photocatalysts [9] as well as their applications in electrochemical [10], optical [11], and electronic devices [12]. Metal oxides, such as TiO_2 , WO_x , and CeO_2 , in combination with Pt, can effectively promote methanol electrooxidation and show significant tolerance to CO poisoning. The enhanced catalytic behavior of the composite catalysts is ascribed to synergistic effects between the oxides and Pt, similar to the bifunctional mechanism [13]. Among other low-cost oxides, Fe_2O_3 nanoparticles may be used as a catalyst support material because of their excellent physicochemical properties, such as high surface area and sizable surface defects. Dhavale et al. [14] synthesized a high-performance core–shell $\text{Fe}_2\text{O}_3/\text{Pt}$ electrocatalyst for oxygen reduction at significantly low Pt loadings.

Iron oxide nanoparticles in the amorphous state are more interesting than their crystallized counterparts when used as a catalyst because the former can form dangling bonds and yield higher surface–bulk ratios [15]. More importantly, amorphous iron oxides do not exhibit the long-range order characteristic of a crystal. The short-range orders of these nanoparticles at the atomic length scale are due to the nature of chemical bonding in the particles. The lattice defects of nanoparticles have distinct implications for mediating atomic arrangement as well as tuning the electronic structure and coordination of the outer shell [16–18]. Based on this concept, arranging Pt as thin shells on an amorphous iron oxide core may improve its catalytic performance. Amorphous iron oxide efficiently stabilizes Pt particle dispersion, which increases the active surface area per weight of Pt and ensures the availability of sufficient OH_{ads} species at lower overpotentials to allow oxidation of the majority of adsorbed poisoning species (e.g., CO) on Pt during methanol electrooxidation. Metal oxides may also interact with the Pt shell by quantizing Pt energy bands or changing the bonding coordination on the Pt shell, which has an important function in CO_{ads} electrooxidation. The core of amorphous iron oxide nanoparticles has an especially significant impact on epitaxial heterogeneous growth on the particle surface. The core may cause short-range or even long-range disorder in the arrangement of Pt atoms and facilitate the development and formation of microcrystalline Pt thin films. Thus, amorphous iron oxides are promising additives for Pt catalysts. Core–shell structural catalysts for MOR have been widely investigated by several research groups. However, to the best of our knowledge, few studies have been conducted on methanol electrooxidation using core–shell $\text{Fe}_2\text{O}_3/\text{Pt}$ catalysts. Furthermore, these studies do not discuss the influence of amorphous iron oxide as cores on Pt shell. As such, research on the synthesis and catalytic activities of core–shell $\text{Fe}_2\text{O}_3/\text{Pt}$ nanoparticles with amorphous iron oxide cores will be of considerable value.

This work reports a facile route for synthesizing core–shell $\text{Fe}_2\text{O}_3/\text{Pt}$ nanoparticles with amorphous Fe_2O_3 cores with focus on cost and activity. The Fe/Pt atomic ratios used were varied from 1/1 to 4/1. Core–shell $\text{Fe}_2\text{O}_3/\text{Pt}$ nanoparticles showed better catalytic performance for MOR than the E-TEK 40 wt% Pt/C catalyst. The microstructures of the as-prepared nanoparticles were also investigated.

2. Experimental methods

2.1. Chemicals and materials

Analytical-grade platinum chloride (PtCl_2 , 99.9%), ferrous chloride ($\text{FeCl}_2 \cdot 4\text{H}_2\text{O}$, 99.9%), tetra-*n*-octylammonium bromide (TOAB), tetrahydrofuran (THF, 99.99%), methanol (99.99%), acetone (99.99%),

ethanol (99.99%), and sulfuric acid (98%) were obtained from Aldrich and Sigma–Aldrich. PtCl_2 and FeCl_2 were used as precursors for producing Fe_2O_3 nanoparticles and core–shell $\text{Fe}_2\text{O}_3/\text{Pt}$ nanoparticles. Lithium triethylborohydride solution ($\text{LiB}(\text{C}_2\text{H}_5)_3\text{H}$, 1 M in THF) was purchased from J&K Scientific Ltd. and used as reductant. Nafion[®] ionomer, a 5% solution of Nafion perfluorinated ion-exchange resin in a mixture of aliphatic low molecular weight alcohols (isopropanol:*n*-propanol at a weight ratio of 55:45) and water (15 wt% to 25 wt% in mixture), was supplied by Aldrich. Carbot Corporation provided the Vulcan XC-72 carbon black (BET: $237 \text{ m}^2 \text{ g}^{-1}$). All chemicals and materials were used without further purification. We prepared all aqueous solutions with ultra-pure water (Milli-Q, Millipore). High-performance 40% Pt supported on Vulcan XC-72 carbon black (Pt/C electrocatalyst) was purchased from BASF E-TEK Corp. and used for comparative analysis.

2.2. Nanoparticle synthesis

Core–shell $\text{Fe}_2\text{O}_3/\text{Pt}$ nanoparticles were synthesized by the two-step chemical reduction of the desired metallic precursor in liquid organic medium (Fig. 1). Briefly, 0.2 mmol FeCl_2 and 0.5 mmol TOAB were dissolved in 10 mL of THF in a three-neck round-bottom flask under flowing argon gas. $\text{LiB}(\text{C}_2\text{H}_5)_3\text{H}$ solution (6 mL) was added dropwise into the mixture under an argon atmosphere at 25 °C. After ~30 s, the solution turned black. The mixture was sonicated for 30 min to reduce Fe^{2+} to Fe nanoparticles. The synthesized Fe nanoparticles in the solution were bubbled under flowing air at 60 °C for 15 min to obtain Fe_2O_3 . Follow, a solution containing 10 mL of THF and an appropriate amount of PtCl_2 were added dropwise to the Fe_2O_3 suspension to deposit a Pt layer on the surface of the Fe_2O_3 nanoparticles by excess reductant at 25 °C under flowing argon gas. After 60 min of sonication, the suspension was separated by centrifugation at 8000 rpm for 10 min. The solid product was washed in THF and ultra-pure water several times and dried at 80 °C for 12 h. Four core–shell $\text{Fe}_2\text{O}_3/\text{Pt}$ nanoparticles with Fe:Pt atomic ratios of 1:1, 2:1, 3:1, and 4:1 were synthesized through this process by varying the amount of added PtCl_2 . The samples were labeled as $\text{Fe}_2\text{O}_3/\text{Pt}$ -a (Fe:Pt = 1:1), $\text{Fe}_2\text{O}_3/\text{Pt}$ -b (Fe:Pt = 2:1), $\text{Fe}_2\text{O}_3/\text{Pt}$ -c (Fe:Pt = 3:1), and $\text{Fe}_2\text{O}_3/\text{Pt}$ -d (Fe:Pt = 4:1). Fe_2O_3 nanoparticles were also prepared by a similar method and labeled Fe_2O_3 -e.

2.3. Electrode preparation

The samples under study were deposited onto a working electrode using ink. The working electrode was a glassy carbon rotating disk electrode (RDE, Hochtemperatur-Werkstoffe GmbH, Germany) with a diameter of 3 mm and electrode area of 0.07 cm^2 . The electrode surface was cleaned to a mirror-finish with alumina slurry and washed with acetone and ultra-pure water before each experiment. Then, 2 mg of the as-prepared nanoparticles was mixed with 3 mg of Vulcan XC-72 carbon black in 5 mL of ultra-pure water. The mixture was stirred using an ultrasonic crusher for 15 min to form a homogenous ink. The ink (6.0 μL) was transferred onto the freshly polished electrode using a microsyringe and dried at 60 °C for 30 min to produce a homogenous coating. To improve mechanical durability and stability, 7.2 mL of 0.5% Nafion[®] solution was added onto the coating surface and dried at 60 °C for 30 min to yield a uniform thin film of catalyst electrode. The real Pt loadings for $\text{Fe}_2\text{O}_3/\text{Pt}$ -a, $\text{Fe}_2\text{O}_3/\text{Pt}$ -b, $\text{Fe}_2\text{O}_3/\text{Pt}$ -c, and $\text{Fe}_2\text{O}_3/\text{Pt}$ -d nanoparticles on the glassy carbon electrodes were maintained at 24.32, 18.84, 15.37, and 12.99 $\mu\text{g cm}^{-2}$, respectively. For comparison, the E-TEK 40 wt% Pt/C catalyst electrode was prepared by a similar method, the Pt loading was maintained at 34.29 $\mu\text{g cm}^{-2}$.

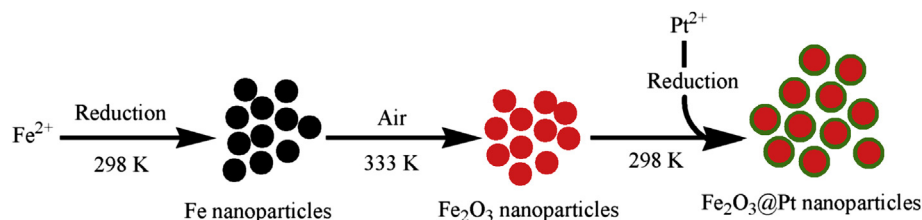


Fig. 1. Formation process of core-shell structured Pt layer coated amorphous Fe_2O_3 nanoparticles.

2.4. Physical characterization

The morphology of the samples was characterized by a Tecnai G2-F20 field emission transmission electron microscope (TEM) at 200 kV. Powder X-ray diffraction (XRD) patterns were obtained using a D/max-2700 X-ray diffractometer operating with $\text{Cu K}\alpha$ radiation ($\lambda = 0.154056 \text{ nm}$) at 40 kV and 30 mA. The XRD profiles were recorded at a scanning rate of 8° min^{-1} . Diffraction peaks were assigned according to the International Center for Diffraction Data cards in the PDF-2 database. Bulk compositional analysis was conducted using an energy dispersive spectroscope (EDS) as a scanning electron microscope accessory. The surface compositions of the $\text{Fe}_2\text{O}_3/\text{Pt}$ nanoparticles and chemical states of the surface Pt atoms in the $\text{Fe}_2\text{O}_3/\text{Pt}$ nanoparticles were characterized by experimental X-ray photoelectron spectroscopy (XPS) with an XSAM800 instrument (Kratos, UK) fitted with an $\text{Al K}\alpha$ ($h\nu = 1486.7 \text{ eV}$) 180 W X-ray source.

2.5. Electrochemical characterization

Electrochemical measurements were performed with a multi-channel VMP3B-20 (Princeton Applied Research) potentiostat controlled by EC-Lab software and the typical setup of a three-electrode electrochemical system. The cell was a 50 mL glass vial that had been treated with $\text{H}_2\text{SO}_4\text{--HNO}_3$ solution and washed with ultra-pure water before each experiment. The working electrode was an RDE. A Pt coil (BAS Instruments, USA) was used as the counter electrode. The reference electrode was a K_2SO_4 saturated $\text{Hg}/\text{Hg}_2\text{SO}_4$ electrode (MSE, BAS Instruments, USA). This electrode was placed as close as possible to the working electrode. All potentials are reported as E versus (MSE)/V. The electrolyte used for the electrochemical measurements was 0.5 M H_2SO_4 . To dispel slight contaminations from the Nafion and study the methanol electrooxidation process, a series of cyclic voltammetry (CV) experiments were conducted. The electrolyte was purged with nitrogen for 30 min to deaerate the system before each CV measurement. The electrodes were cycled at 50 mV s^{-1} between -0.65 and 0.7 V until reproducible cyclic voltammograms were obtained. These voltammograms indicated that the catalysts were stable under the experimental conditions. The electrocatalytic characteristics of all samples were studied by CV, chronoamperometry, and in situ Fourier transform infrared (FTIR) reflectance spectroscopy in N_2 -saturated $1.0 \text{ M CH}_3\text{OH} + 0.5 \text{ M H}_2\text{SO}_4$ solutions at room temperature.

Spectro-electrochemical measurements were performed by in situ FTIR spectroscopy (Thermo Electron Corporation, USA) using a Nicolet 6700 FTIR spectrometer equipped with a mercury–cadmium–telluride detector cooled with liquid nitrogen and a thin-layer infrared (IR) cell with an array of catalyst electrodes. A CaF_2 disk was used as the IR window, and a thin layer of solution was formed by moving the array of catalyst electrodes during in situ FTIR spectroscopy measurements. A single potential alternation FTIR procedure [19] was performed to investigate methanol

oxidation. The electrode potential was maintained at 0.70 V for 5 s to clean the surface of the working electrode and remove any adsorbates by oxidation. The potential was then switched to -0.65 V for 2 min to refresh the thin layer of solution. The resulting spectrum was calculated using Eq. (1) [20]:

$$\frac{\Delta R}{R}(E_S) = \frac{R(E_S) - R(E_R)}{R(E_R)} \quad (1)$$

where $R(E_R)$ and $R(E_S)$ are the reference single-beam spectrum and sample single-beam spectrum, respectively. Each single-beam spectrum was acquired by collecting and co-adding 300 interferograms at a spectral resolution of 16 cm^{-1} .

3. Results and discussion

3.1. Physical and chemical analysis

Fig. 2 displays the XRD patterns of the Fe_2O_3 and $\text{Fe}_2\text{O}_3/\text{Pt}$ nanoparticles. The characteristic diffraction peaks of Fe_2O_3 are not detected in the Fe_2O_3 nanoparticles, indicating that the Fe_2O_3 nanoparticles have an amorphous structure. This result is consistent with previous findings [21]. The amorphous structure of the Fe_2O_3 cores has a significant effect on the catalytic activity of the core-shell $\text{Fe}_2\text{O}_3/\text{Pt}$ nanoparticles. The peaks located at $2\theta = 39.76^\circ$, 46.24° , and 67.45° respectively correspond to the (111), (200), and (220) lattice planes of Pt (JCPDS, No. 04-0802). Typical peaks characteristic of the face-centered cubic lattice structure of the Pt shell in $\text{Fe}_2\text{O}_3/\text{Pt}$ -a are observed. The XRD patterns of the $\text{Fe}_2\text{O}_3/\text{Pt}$ -a and $\text{Fe}_2\text{O}_3/\text{Pt}$ -b samples show peaks corresponding to Pt

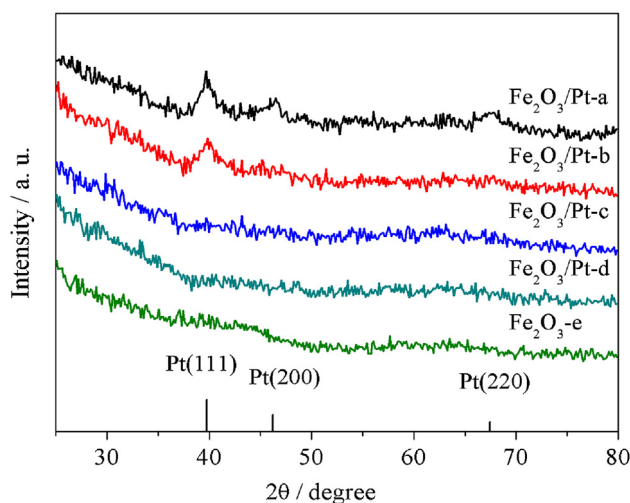


Fig. 2. Powder XRD patterns of Fe_2O_3 and the core-shell $\text{Fe}_2\text{O}_3/\text{Pt}$ nanoparticles: $\text{Fe}_2\text{O}_3/\text{Pt}$ -a (Fe:Pt = 1:1), $\text{Fe}_2\text{O}_3/\text{Pt}$ -b (Fe:Pt = 2:1), $\text{Fe}_2\text{O}_3/\text{Pt}$ -c (Fe:Pt = 3:1), $\text{Fe}_2\text{O}_3/\text{Pt}$ -d (Fe:Pt = 4:1), Fe_2O_3 -e.

without any noticeable shift. This result indicates that the products are not Fe–Pt alloys, which exhibit diffraction peaks between Fe and Pt [22]. Furthermore, the diffraction peak intensity of Pt gradually decreases with decreasing Pt contents in the $\text{Fe}_2\text{O}_3/\text{Pt}$ nanoparticles. For Fe/Pt atomic ratios larger than 2:1, the diffraction peak of Pt is not observed, possibly because the Pt shell loaded in the amorphous Fe_2O_3 surface in the crystallite has a very small crystal orientation. Amorphous Fe_2O_3 has many lattice defects that can significantly affect epitaxial heterogeneous growth on the particle surface. This effect is not conducive to the directional arrangement of Pt atoms and results in the development and formation of a microcrystalline Pt thin film. Therefore, this phenomenon should be investigated to improve the properties of Pt catalysts.

Fig. 3 displays the XPS spectra of the core–shell $\text{Fe}_2\text{O}_3/\text{Pt}$ nanoparticles in the Fe 2p and Pt 4f regions. The binding energy (BE) scale was calibrated by measuring the C 1s peak (BE = 284.2 eV). Overlapping peaks were deconvoluted, and the peaks were identified as different oxidation states. In Fe 2p region, the peak positions at 711 and 724 eV for Fe 2p_{3/2} and Fe 2p_{1/2} may be assigned to Fe^{3+} in Fe_2O_3 . No characteristic peaks around 707 and 720 eV for Fe 2p_{3/2} and Fe 2p_{1/2} belonging to metallic iron [14,17]. This result shows that the cores of the nanoparticles predominantly present as Fe_2O_3 . In Pt 4f region, the peaks around 71 and 74 eV may be assigned to the Pt 4f_{7/2} and Pt 4f_{5/2} of metallic platinum. The peaks present at higher BE correspond to Pt^{2+} in $\text{PtO}/\text{Pt}(\text{OH})_2$ (72 and 75 eV) and Pt^{4+} in PtO_2 (74 and 77 eV) species in the composites. Pt is predominantly present as metallic Pt along with surface oxides and hydroxide as is commonly observed in the case of ultrafine Pt particles [23]. The Pt 4f_{7/2} BE corresponds to metallic Pt for $\text{Fe}_2\text{O}_3/\text{Pt}$ -a, $\text{Fe}_2\text{O}_3/\text{Pt}$ -b, $\text{Fe}_2\text{O}_3/\text{Pt}$ -c, and $\text{Fe}_2\text{O}_3/\text{Pt}$ -d nanoparticles located at 71.30, 71.35, 71.50, and 71.55 eV, respectively. Compared with bulk Pt (71.20 eV) [24], the Pt in the $\text{Fe}_2\text{O}_3/\text{Pt}$ nanoparticles has higher BE values. The upshift of the Pt BE may be attributed to the effect of the amorphous Fe_2O_3 cores. Moreover, Pt BE increases with decreasing Pt contents. Larger Fe/Pt atomic ratios result in higher Pt BE, implying that the electronic structure of Pt is modified when it is deposited on the surface of amorphous Fe_2O_3 nanoparticles. The electronic effect between Pt and Fe_2O_3 increases with decreasing Pt contents in the $\text{Fe}_2\text{O}_3/\text{Pt}$ nanoparticles.

Fig. 4 shows the TEM images of unsupported $\text{Fe}_2\text{O}_3/\text{Pt}$ nanoparticles with Fe/Pt atomic ratio of 2:1. The as-prepared $\text{Fe}_2\text{O}_3/\text{Pt}$ nanoparticles have near-spherical shapes and show slight agglomeration. Considering their very small particle size, the as-prepared $\text{Fe}_2\text{O}_3/\text{Pt}$ nanoparticles agglomerated because of their excellent magnetic property [25]. The core and shell components of the $\text{Fe}_2\text{O}_3/\text{Pt}$ nanoparticles can be easily identified by brightness differences. The dark Fe_2O_3 cores have an average diameter of 3 nm. The atomic ratios of Fe:Pt in the $\text{Fe}_2\text{O}_3/\text{Pt}$ -a, $\text{Fe}_2\text{O}_3/\text{Pt}$ -b, $\text{Fe}_2\text{O}_3/\text{Pt}$ -c, and $\text{Fe}_2\text{O}_3/\text{Pt}$ -d nanoparticles determined by EDS are listed in Table 1. These data are consistent with the molar ratio in the starting precursor salts, indicating that the strong reducing agent $\text{LiB}(\text{C}_2\text{H}_5)_3\text{H}$ can fully reduce Fe^{2+} and Pt^{2+} under the adopted experimental conditions. For comparison, the surface Fe:Pt atomic ratios in $\text{Fe}_2\text{O}_3/\text{Pt}$ nanoparticles determined by XPS are also listed in Table 1. The results indicate that the atomic content Fe/Pt ratios are remarkably lower than the corresponding bulk atomic content Fe/Pt ratios measured by EDS, which may be ascribed to the photoelectron attenuation lengths ranging from approximately 2 nm to 5 nm. This result further confirms the presence of a Pt-rich shell around the Fe_2O_3 core.

3.2. Electrochemical analysis

To understand the core–shell structure of the $\text{Fe}_2\text{O}_3/\text{Pt}$ nanoparticles, a series of nanoparticle catalysts are examined by CV in 0.5 M H_2SO_4 solution. The Pt/C catalyst is included for comparison. This technique is sensitive to surface compositions and structures and detects the electrochemical properties of surface atoms rather than bulk atoms [26]. The result is shown in Fig. 5. All $\text{Fe}_2\text{O}_3/\text{Pt}$ nanoparticle catalysts exhibit adsorption/desorption CV characteristics of hydrogen and oxygen very similar to those of Pt/C, i.e., hydrogen evolution zone from -0.65 V to -0.35 V, double layer formation zone from -0.35 V to -0.1 V, and Pt oxidation/reduction zone above -0.1 V. Therefore, these nanoparticles have Pt surfaces, thus confirming earlier TEM results and showing that the prepared nanoparticles possess a $\text{Fe}_2\text{O}_3/\text{Pt}$ core–shell structure. The electrochemically active surface area (EAS) of the catalysts is one of the most important parameters for determining the electrocatalytic activity for methanol oxidation, which occurs on the surface of Pt particles [27]. Based on the monolayer adsorption of hydrogen on the Pt surface, the real EAS of Pt-based catalysts under the

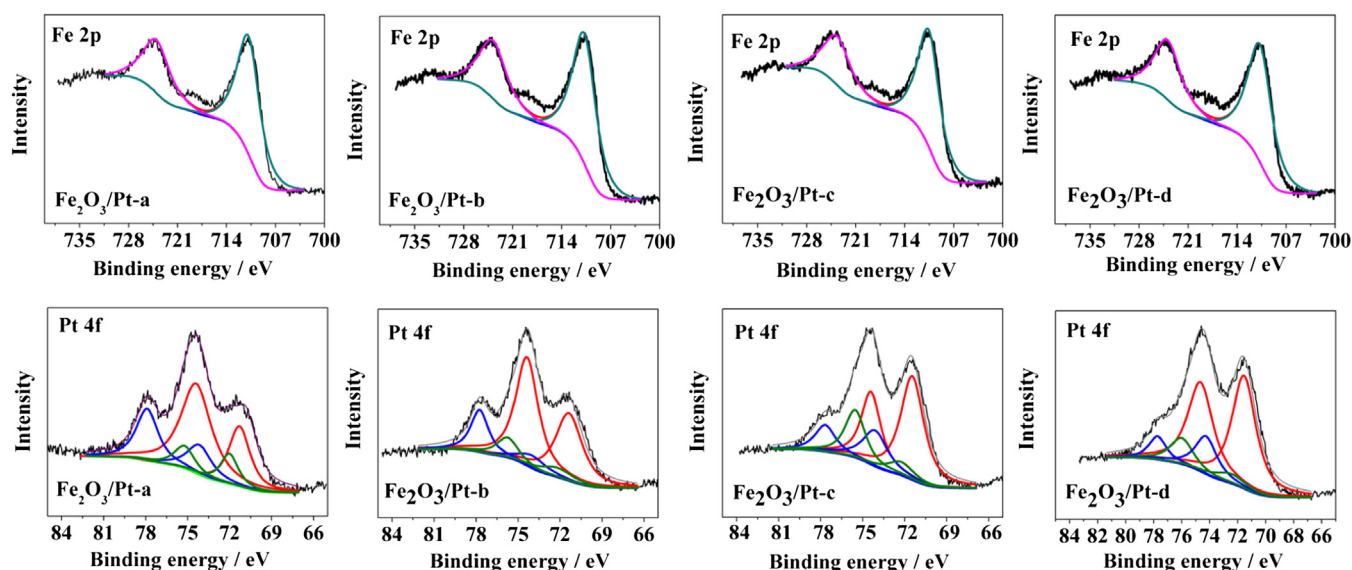


Fig. 3. XPS spectra of $\text{Fe}_2\text{O}_3/\text{Pt}$ -a (Fe:Pt = 1:1), $\text{Fe}_2\text{O}_3/\text{Pt}$ -b (Fe:Pt = 2:1), $\text{Fe}_2\text{O}_3/\text{Pt}$ -c (Fe:Pt = 3:1), and $\text{Fe}_2\text{O}_3/\text{Pt}$ -d (Fe:Pt = 4:1) nanoparticles.

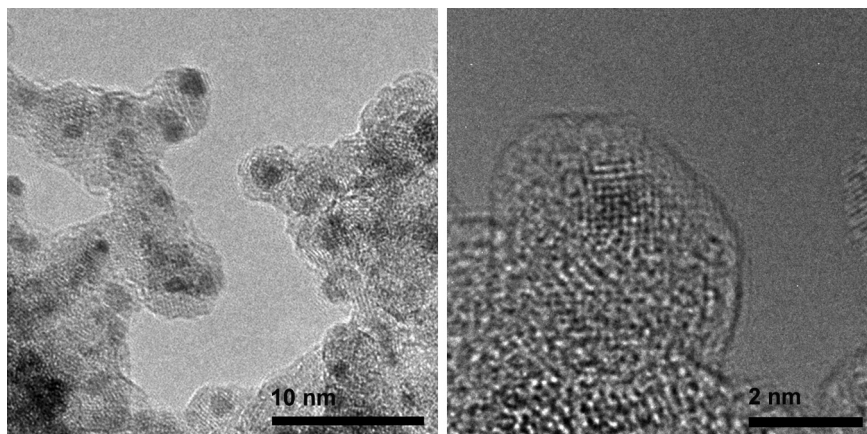


Fig. 4. TEM images of unsupported Fe₂O₃/Pt (Fe:Pt = 2:1) nanoparticles.

hydrogen adsorption/desorption peak can be calculated by integrating the hydrogen desorption region of the CV [28]. The EAS of the different catalysts was calculated using Eq. (2):

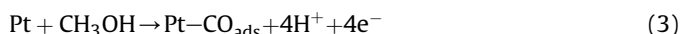
$$A_{EL} = \frac{Q_H}{2.1 \times m_{Pt}} \quad (2)$$

where Q_H is the integral of the hydrogen desorption peak on the Pt surface ($C\ m^{-2}$), 2.1 is the charge required to oxidize a monolayer of hydrogen on the Pt surface ($C\ m^{-2}$), and m_{Pt} is the Pt loading on the glassy carbon electrode ($g\ m^{-2}$) [29–31]. Table 1 presents the calculated EAS value of all catalysts. The EAS of the H₂ desorption peaks are larger for all core–shell catalysts than that for the Pt/C catalyst, indicating better Pt utilization for core–shell nano-structure catalysts than that for the Pt/C catalyst. Therefore, the presence of amorphous iron oxide efficiently enhances the dispersion of Pt particles because of the increased active surface area per weight of Pt.

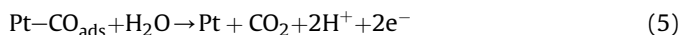
Considering that long-term structural stability is also important for electrocatalysts [32], this property was evaluated in Fe₂O₃/Pt nanoparticles and Pt/C catalyst by continuous CV cycling from −0.65 V to 0.7 V in 0.5 M H₂SO₄ solution at room temperature. Fig. 6 shows the cyclic voltammograms and the evolution of the EAS of all catalysts after an increasing number of potential cycles. The variation in structure stabilities shows the importance of catalyst composition and structure. The EAS of Fe₂O₃/Pt-a and Fe₂O₃/Pt-b slowly decreases with increasing scan cycles, finally maintaining values about ~86% and ~89% of the initial value after 6000 CV cycles. By contrast, the EAS of Fe₂O₃/Pt-d and Pt/C decreases to about ~66% and ~59% of the initial value. This result reveals that the structural stability of the prepared core–shell nanoparticles is much higher than that of the Pt/C catalyst. The core–shell architecture with an amorphous Fe₂O₃ core prevents Pt dissolution, nanoparticle aggregation, and loss of contact to the carbon black support compared with the Pt/C catalyst. The significant decrease

in EAS in the Fe₂O₃/Pt-d sample may be attributed to the dissolution of amorphous Fe₂O₃ because the Pt shell is too thin to completely cover the amorphous Fe₂O₃ core.

Fig. 7 presents the Pt loading mass-normalized cyclic voltammograms for all of the catalysts in 0.5 M H₂SO₄ + 1.0 M CH₃OH solution. The voltammograms exhibit markedly different voltammetric features in terms of oxidation peak potential and specific activity. Two representative oxidation peaks are investigated. The first one is between −0.1 and 0.4 V in the forward scan (peak 1) and the second is between −0.3 and 0.2 V in the backward scan (peak 2). The current peak for the forward scan (j_f) is ascribed to the oxidation of freshly chemisorbed species originating from methanol dissociative adsorption, forming Pt-adsorbed carbonaceous species including CO and CO₂. This adsorbed CO poisons the catalyst. The reactions can be expressed as follows ((3) and (4)) [33]:



The current peak for the backward scan (j_b) is primarily associated with the removal of carbonaceous species that are not completely oxidized in the forward sweep and caused by freshly chemisorbed species [34–36], as shown in reaction (5).



Based on the above deduction, the ratio j_f/j_b is used to describe the tolerance to incompletely oxidized species accumulated on the surface of the electrode. A higher ratio indicates more effective removal of poisonous carbonaceous species on the catalyst surface [37,38]. The values of the onset potential (E_{onset}), peak potential (E_p), maximum current density (normalized by EAS and Pt loading mass), and ratio j_f/j_b of all of the catalysts are listed in Table 1. The peak potentials in the positive-direction scan of all Fe₂O₃/Pt catalysts are lower than that of Pt/C, indicating the facile reaction

Table 1

Fe/Pt atomic ratios and cyclic voltammogram features of the as-prepared core–shell Fe₂O₃/Pt nanoparticles and the Pt/C catalyst.

Catalyst	Fe:Pt atomic ration determined by EDS	Fe:Pt atomic ration determined by XPS	EAS ($m^2\ g^{-1}\ Pt$)	E_{onset} (V)	E_p (V)	Current density ($mA\ cm^{-2}$)	J_f ($A\ mg^{-1}\ Pt$)	J_b ($A\ mg^{-1}\ Pt$)	j_f/j_b
Fe ₂ O ₃ /Pt-a	1.13:1	0.63:1	37.39	−0.13	0.19	1.39	0.80	0.69	1.16
Fe ₂ O ₃ /Pt-b	2.21:1	1.17:1	42.56	−0.14	0.18	2.21	1.26	1.08	1.17
Fe ₂ O ₃ /Pt-c	3.17:1	2.01:1	56.15	−0.13	0.19	2.31	0.98	0.82	1.20
Fe ₂ O ₃ /Pt-d	4.26:1	2.45:1	57.76	−0.13	0.18	1.91	0.71	0.60	1.18
Pt/C E-TEK	/	/	30.51	−0.16	0.24	1.48	0.45	0.56	0.80

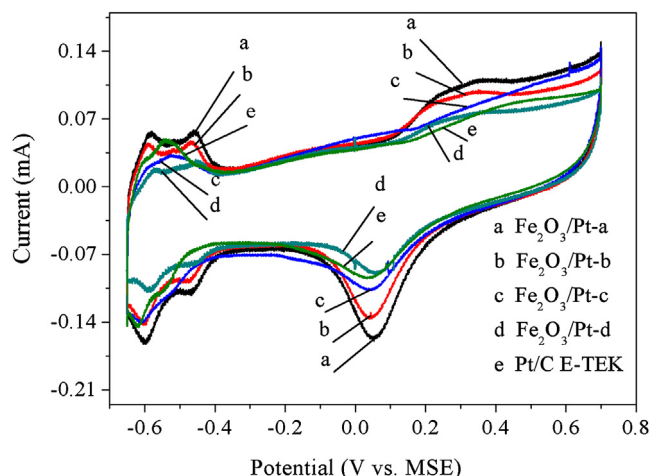


Fig. 5. Cyclic voltammograms of $\text{Fe}_2\text{O}_3/\text{Pt}$ -a (Fe:Pt = 1:1), $\text{Fe}_2\text{O}_3/\text{Pt}$ -b (Fe:Pt = 2:1), $\text{Fe}_2\text{O}_3/\text{Pt}$ -c (Fe:Pt = 3:1), $\text{Fe}_2\text{O}_3/\text{Pt}$ -d (Fe:Pt = 4:1) and Pt/C catalysts in N_2 -saturated 1.0 M CH_3OH + 0.5 M H_2SO_4 solutions, scan rate: 50 mV s^{-1} .

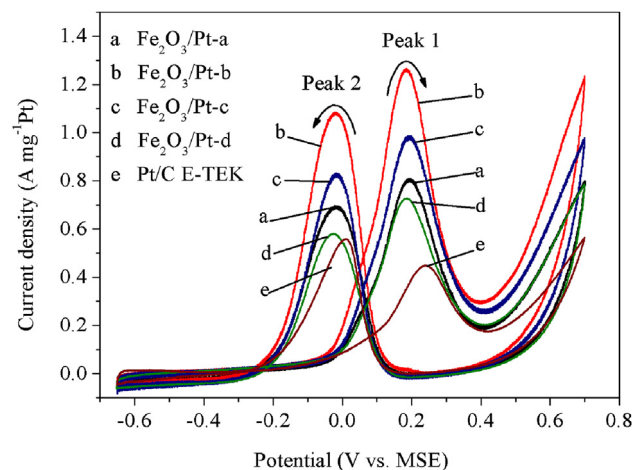


Fig. 7. Cyclic voltammograms of $\text{Fe}_2\text{O}_3/\text{Pt}$ -a (Fe:Pt = 1:1), $\text{Fe}_2\text{O}_3/\text{Pt}$ -b (Fe:Pt = 2:1), $\text{Fe}_2\text{O}_3/\text{Pt}$ -c (Fe:Pt = 3:1), $\text{Fe}_2\text{O}_3/\text{Pt}$ -d (Fe:Pt = 4:1), and Pt/C catalysts in N_2 -saturated 1.0 M CH_3OH + 0.5 M H_2SO_4 solutions, scan rate: 50 mV s^{-1} .

kinetics for methanol dehydrogenation of these core-shell $\text{Fe}_2\text{O}_3/\text{Pt}$ catalysts. The electrocatalytic activity of all core-shell structured Pt-rich shell-coated amorphous Fe_2O_3 nanoparticles is significantly improved compared with that of the Pt/C catalyst. The current density and tolerance for carbonaceous species poisoning of the $\text{Fe}_2\text{O}_3/\text{Pt}$ nanoparticles first increase and then decrease as the Pt content decreases, which contradicts the change trend of the EAS of Pt. Thus, the enhanced electrocatalytic activity of the core-shell $\text{Fe}_2\text{O}_3/\text{Pt}$ catalyst is associated with its improved Pt utilization as well as the electronic effect between Fe_2O_3 and Pt. Among the nanoparticles studied, $\text{Fe}_2\text{O}_3/\text{Pt}$ -b (Fe:Pt = 2:1) has the highest specific mass activity, which is approximately 3 times that of Pt/C. The EAS catalytic activity of $\text{Fe}_2\text{O}_3/\text{Pt}$ -c (Fe:Pt = 3:1) is the highest

($\sim 2.31 \text{ mA cm}^{-2}$) among the samples, which is approximately 1.56 times that of Pt/C. The $j_{\text{an}}/j_{\text{c}}$ ratios of all core-shell $\text{Fe}_2\text{O}_3/\text{Pt}$ catalysts are also higher than that of the Pt/C catalyst, which indicates that core-shell $\text{Fe}_2\text{O}_3/\text{Pt}$ catalysts have better tolerance to intermediates than the Pt/C catalyst. The enhanced performance of the core-shell Fe-Pt catalysts, especially $\text{Fe}_2\text{O}_3/\text{Pt}$ -b (Fe:Pt = 2:1) and $\text{Fe}_2\text{O}_3/\text{Pt}$ -c (Fe:Pt = 3:1), may be due to chemical and structural effects. Pt catalytic activity for MOR can be enhanced by the electronic effects of two metals [5]. Furthermore, the higher dispersion and utilization of Pt can be achieved when Pt is deposited on the surface of the nanoparticle core [39,40]. The electrochemical oxidation of the carbonaceous intermediate can also be promoted by amorphous Fe_2O_3 cores.

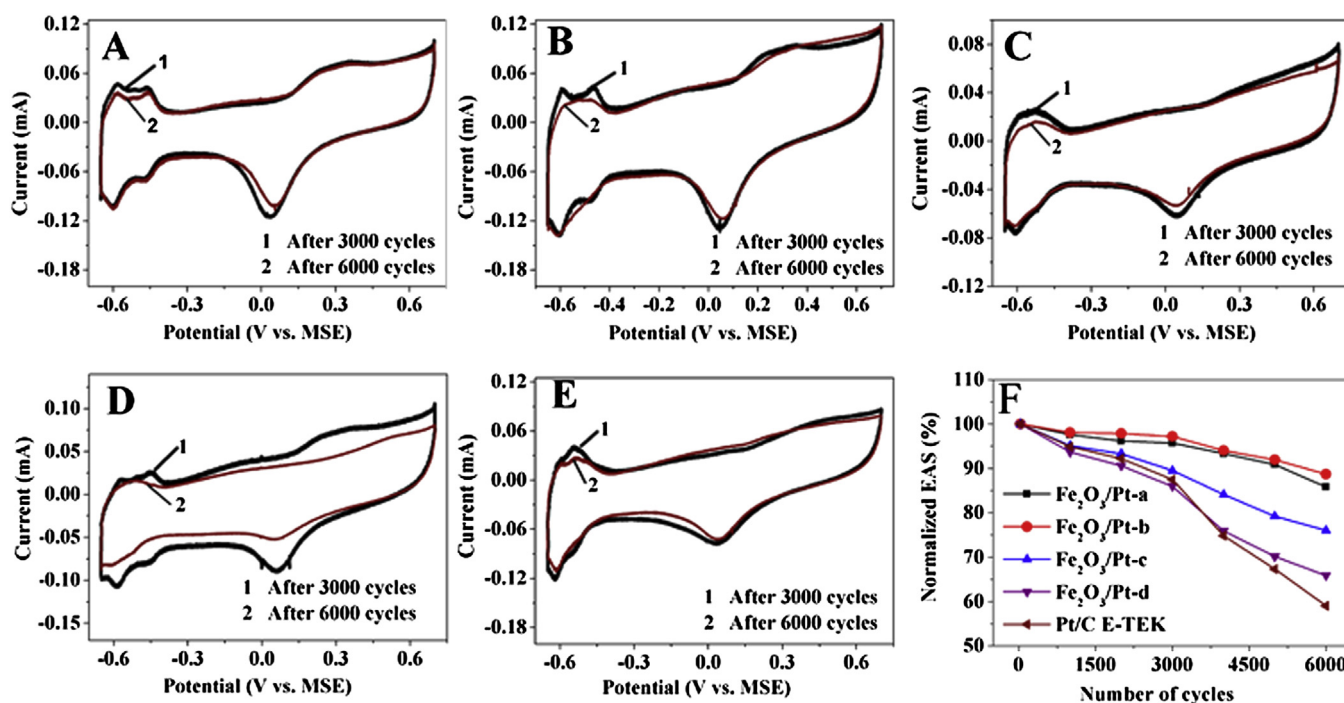


Fig. 6. Cyclic voltammograms of (A) $\text{Fe}_2\text{O}_3/\text{Pt}$ -a (Fe:Pt = 1:1), (B) $\text{Fe}_2\text{O}_3/\text{Pt}$ -b (Fe:Pt = 2:1), (C) $\text{Fe}_2\text{O}_3/\text{Pt}$ -c (Fe:Pt = 3:1), (D) $\text{Fe}_2\text{O}_3/\text{Pt}$ -d (Fe:Pt = 4:1) and (E) Pt/C catalysts after various numbers of potential cycles. (F) The loss of EAS of different catalysts after cycling for 6000 CVs between -0.65 and 0.7 V in N_2 -saturated 1.0 M CH_3OH + 0.5 M H_2SO_4 solutions, scan rate: 50 mV s^{-1} .

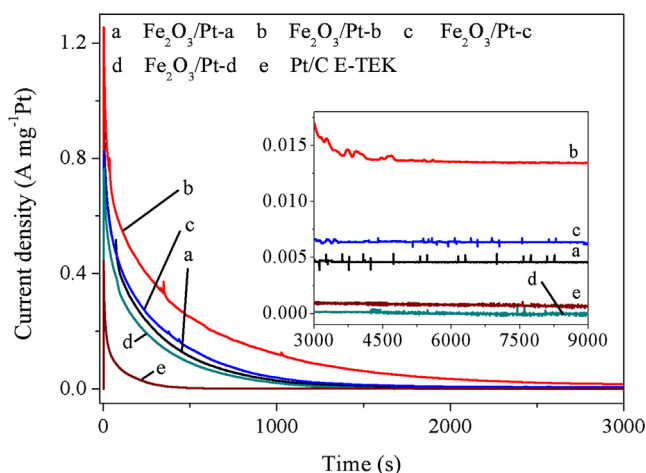


Fig. 8. Chronoamperometric curves of N_2 -saturated 1.0 M CH_3OH + 0.5 M H_2SO_4 solutions at $\text{Fe}_2\text{O}_3/\text{Pt}$ -a (Fe:Pt = 1:1), $\text{Fe}_2\text{O}_3/\text{Pt}$ -b (Fe:Pt = 2:1), $\text{Fe}_2\text{O}_3/\text{Pt}$ -c (Fe:Pt = 3:1), $\text{Fe}_2\text{O}_3/\text{Pt}$ -d (Fe:Pt = 4:1), and Pt/C catalyst electrodes for 9000 s; fixed potential: 0.2 V.

Evaluation of long-term catalytic activity is important for the practical application of electrocatalysts [41]. To confirm the long-term performance of the core-shell $\text{Fe}_2\text{O}_3/\text{Pt}$ catalysts for methanol oxidation, a chronoamperometry test at 0.2 V versus the MSE was conducted for a period of 9000 s. Fig. 8 shows the chronoamperometry curves for all catalysts in 0.5 M H_2SO_4 + 1.0 M CH_3OH solution. At short testing times, the oxidation current rapidly decays for all catalysts possibly because of catalyst poisoning by intermediate species, such as CO_{ads} , $\text{CH}_3\text{OH}_{\text{ads}}$, CHO_{ads} , and OH_{ads} , which form during methanol oxidation reaction [42]. After 2000 s, the rate of current decay gradually slows and remains pseudo-stable. This long-term current decay is due to the accumulation of CO-like species on the catalyst surfaces, which is caused by the decomposition of methanol molecules. Surface-adsorbed SO_4^{2-} anions on the catalysts also lead to current decay by restricting the reaction active sites [43,44]. The chronoamperograms obtained were used to obtain the rate of long-term poisoning (δ) of the catalysts, which is expressed as the percentage of poisoned catalyst per second ($\% \text{ s}^{-1}$) [45,46], using the following equation (6):

$$\delta = \frac{100}{J_0} \times \left(\frac{dJ}{dt} \right) \quad (6)$$

where dJ/dt is the slope of the linear portion of the current decay, and J_0 is the current at the start of polarization back extrapolated from the linear current decay. The percentage of poisoning for all catalysts is listed in Table 2. $\text{Fe}_2\text{O}_3/\text{Pt}$ -b (Fe:Pt = 2:1) and $\text{Fe}_2\text{O}_3/\text{Pt}$ -c (Fe:Pt = 3:1) catalysts present higher resistance to poisoning of active sites for methanol electrooxidation than the three other catalysts. This result indicates that core-shell $\text{Fe}_2\text{O}_3/\text{Pt}$ nanoparticles can significantly enhance the catalytic durability of Pt, consistent with the results of the long-term structure stability measurements (Fig. 6). The enhanced long-term performance of the core-shell $\text{Fe}_2\text{O}_3/\text{Pt}$ catalysts is attributed to two main reasons. First, the presence of amorphous Fe_2O_3 cores modifies the dispersion and electronic structure of Pt and influences the chemi-adsorption of methanol and poisoning species, such as CO. Second, amorphous iron oxide nanoparticles facilitate the development and formation of a microcrystalline Pt thin film, which strongly influences surface atom densities and chemical reactivity.

Characterization of methanol oxidation by the CV technique cannot directly indicate whether or not the CO_{ads} species derived

Table 2

Percentage of poisoning after 9000 s for 1.0 M methanol electrooxidation on core-shell $\text{Fe}_2\text{O}_3/\text{Pt}$ catalysts and Pt/C.

Catalyst	$J_{\text{polarization}}$ (μA)	J_{final} (μA)	$t_{\text{polarization}}$ (s)	$(dJ/dt)_{t=9000 \text{ s}}$	δ ($\% \text{ s}^{-1}$)
$\text{Fe}_2\text{O}_3/\text{Pt}$ -a	15.70	11.70	2000	$5.71\text{E-}04$	$3.64\text{E-}03$
$\text{Fe}_2\text{O}_3/\text{Pt}$ -b	22.13	20.56	3500	$2.85\text{E-}04$	$1.29\text{E-}03$
$\text{Fe}_2\text{O}_3/\text{Pt}$ -c	6.35	5.71	2000	$9.14\text{E-}05$	$1.44\text{E-}03$
$\text{Fe}_2\text{O}_3/\text{Pt}$ -d	0.37	0.10	2000	$3.86\text{E-}05$	$1.04\text{E-}02$
Pt/C E-TEK	2.38	1.47	2000	$1.14\text{E-}04$	$4.78\text{E-}03$

from methanol acts as a poison by inhibiting methanol oxidation. Thus, we used in situ FTIR spectroscopy to further examine the methanol oxidation process on various catalyst electrodes. Fig. 9 shows the in situ FTIR reflectance spectra of methanol oxidation on the core-shell $\text{Fe}_2\text{O}_3/\text{Pt}$ catalysts and Pt/C at 0.20 V in 0.5 M H_2SO_4 + 1.0 M CH_3OH solution. The upward bands centered at approximately 2070 cm^{-1} are ascribed to the IR absorption of linear-bonded CO. The smaller feature band around 1890 cm^{-1} is assigned to the bridged form of CO [47]. The downward doublet peaks centered at about 2330 and 2360 cm^{-1} are attributed to the production of CO_2 . This band reflects the cleavage of the C–H bond for methanol oxidation. More CO_2 and less CO are obviously formed on the core-shell $\text{Fe}_2\text{O}_3/\text{Pt}$ catalysts during methanol oxidation than on the Pt/C catalyst. The in situ FTIR results clearly indicate that the core-shell $\text{Fe}_2\text{O}_3/\text{Pt}$ catalysts, especially $\text{Fe}_2\text{O}_3/\text{Pt}$ -b (Fe:Pt = 2:1) and $\text{Fe}_2\text{O}_3/\text{Pt}$ -c (Fe:Pt = 3:1), feature enhanced reactivity for breaking the C–H bond in methanol compared with the Pt/C catalyst. Consequently, they show higher selectivity for the complete oxidation of methanol to CO_2 .

The high MOR activity of the Pt-decorated amorphous Fe_2O_3 nanoparticle electrocatalyst is a counterintuitive observation. Methanol oxidation processes on Pt–M alloys occur by a bifunctional mechanism, in which OH species adsorbed on the highly oxophilic Fe or Ru sites facilitate the oxidation of CO adsorbed on the Pt sites [48,49]. The pure Pt surface of the core-shell $\text{Fe}_2\text{O}_3/\text{Pt}$ nanoparticles with amorphous Fe_2O_3 cores is oxidized through a different mechanism. Composition and structural analyses show that differences in the process of methanol oxidation on these catalysts may be attributed to the interaction between Pt particles and the amorphous Fe_2O_3 substrate. Pt metal– Fe_2O_3 substrate interactions have several effects. First, the core-shell nanostructure

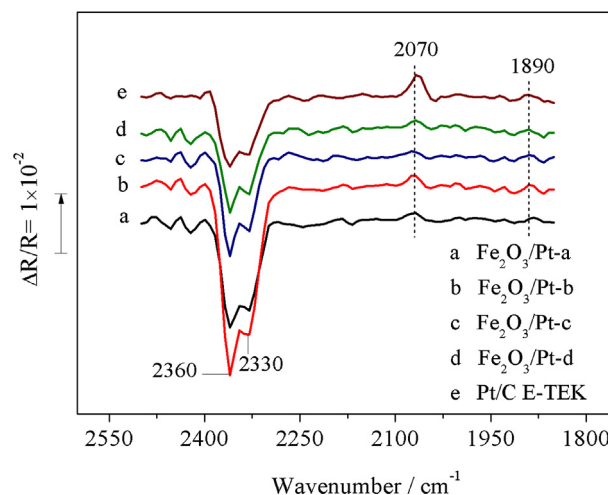


Fig. 9. In situ-FTIR spectra for methanol oxidation on $\text{Fe}_2\text{O}_3/\text{Pt}$ -a (Fe:Pt = 1:1), $\text{Fe}_2\text{O}_3/\text{Pt}$ -b (Fe:Pt = 2:1), $\text{Fe}_2\text{O}_3/\text{Pt}$ -c (Fe:Pt = 3:1), $\text{Fe}_2\text{O}_3/\text{Pt}$ -d (Fe:Pt = 4:1), and Pt/C catalysts in N_2 -saturated 1.0 M CH_3OH + 0.5 M H_2SO_4 solutions, reference spectra collected at -0.65 V .

increases the utilization efficiency of precious metal electrocatalysts. The $\text{Fe}_2\text{O}_3/\text{Pt}$ catalyst has a larger surface area than the Pt/C catalyst and thus provides more active sites for methanol electrooxidation. Second, amorphous Fe_2O_3 is a more oxophilic compound than Pt. The oxidative removal of CO_{ads} on the Pt shell is considerably accelerated by the availability of numerous active oxygen-containing species in the Fe_2O_3 core. Third, the electronic structure of the Pt atoms modified by amorphous Fe_2O_3 results in a positive core level shift of Pt $4f_{7/2}$, which weakens the Pt–CO bond and facilitates dehydrogenation during MOR [50]. Finally, amorphous Fe_2O_3 has many lattice defects that may significantly affect epitaxial heterogeneous growth on the particle surface and yield favorable structural arrangements of Pt atoms on the particle surface, such as more active sites or larger Pt–Pt interatomic distances, during the electrooxidation of methanol.

4. Conclusions

The experimental results obtained in this work show that core–shell $\text{Fe}_2\text{O}_3/\text{Pt}$ nanoparticles with amorphous Fe_2O_3 cores may be successfully synthesized by a two-step chemical reduction method in liquid organic medium. The core–shell structure can be characterized by various physical and electrochemical techniques. Catalytic performance may be tested using MOR as an indicator. All of the core–shell nanoparticles with complete and thin Pt shells on the amorphous Fe_2O_3 core show superior Pt utilization (specific mass activity), tolerance to carbonaceous species poisoning, and higher CO_2 selectivity for methanol oxidation in acidic medium than the E-TEK 40 wt% Pt/C catalyst. Furthermore, the catalytic activity of core–shell $\text{Fe}_2\text{O}_3/\text{Pt}$ nanoparticles first increases and then decreases with decreasing Pt content. This significant improvement in catalytic performance may be attributed to the uniform distribution of Pt particles on the amorphous Fe_2O_3 surface as well as interactions between the Pt particles and amorphous Fe_2O_3 cores.

These findings demonstrate that amorphous iron oxides are excellent substrates for synthesizing core–shell Pt catalysts. This study provides new insights for further developing and designing efficient catalyst materials for DMFC applications.

Acknowledgment

The authors acknowledge the support of research project NSFC (20676088) provided by China National Natural Science foundation.

References

- [1] M. Xu, G. Gao, W. Zhou, K. Zhang, H. Li, J. Power Sources 175 (2008) 217–220.
- [2] V.B. Hughes, R. Miles, J. Electroanal. Chem. 145 (1983) 87–107.
- [3] T. Frelink, W. Visscher, J.A.R. van Veen, J. Electroanal. Chem. 382 (1995) 65–72.

- [4] T.S. Ahmadi, Z.L. Wang, T.C. Green, A. Henglein, M.A. El-Sayed, Science 272 (1996) 1924–1926.
- [5] F. Caruso, Adv. Mater. 13 (2001) 11–22.
- [6] V.R. Stamenkovic, B.S. Mun, K.J.J. Mayrhofer, P.N. Ross, N.M. Markovic, J. Am. Chem. Soc. 128 (2006) 8813–8819.
- [7] I.X. Green, W. Tang, M. Neurock, J.T. Yates, Science 333 (2011) 736–739.
- [8] R.F. Zio, E.P. Giannelis, B.A. Weinstein, M.P. O'Horo, B.N. Ganguly, V. Mehrotra, M.W. Russell, D.R. Huffman, Science 257 (1992) 219–223.
- [9] S. Sato, Science 295 (2002) 626–627.
- [10] R.K. Nagarale, U. Hoss, A. Heller, J. Am. Chem. Soc. 134 (2012) 20783–20787.
- [11] J. Feng, D. Zhang, Y. Liu, Y. Bai, Q. Chen, S. Liu, H. Sun, J. Phys. Chem. C 114 (2010) 6718–6721.
- [12] J.W. Hennek, Y. Xia, K. Everaerts, M.C. Hersam, A. Facchetti, T.J. Marks, ACS Appl. Mater. Interfaces 4 (2012) 1614–1619.
- [13] H. Yuan, D. Guo, X. Qiu, W. Zhu, L. Chen, J. Power Sources 188 (2009) 8–13.
- [14] V.M. Dhavale, S. Kurungot, J. Phys. Chem. C 116 (2012) 7318–7326.
- [15] D.N. Srivastava, N. Perkas, A. Gedanken, I. Felner, J. Phys. Chem. B 106 (2002) 1878–1883.
- [16] H. Cao, S.L. Suib, J. Am. Chem. Soc. 116 (1994) 5334–5342.
- [17] X. Zhang, J. Yan, S. Han, H. Shioyama, Q. Xu, J. Am. Chem. Soc. 131 (2009) 2778–2779.
- [18] J. Yan, X. Zhang, S. Han, H. Shioyama, Q. Xu, Angew. Chem. Int. Ed. 47 (2008) 2287–2289.
- [19] D.S. Corrigan, L.W.H. Leung, M.J. Weaver, Anal. Chem. 59 (1987) 2252–2256.
- [20] J. Li, Q. Chen, S. Sun, Electrochim. Acta 52 (2007) 5725–5732.
- [21] L. Machala, R. Zboril, A. Gedanken, J. Phys. Chem. B 111 (2007) 4003–4018.
- [22] A.R. Malheiro, J. Perez, H.M. Villullas, J. Power Sources 195 (2010) 3111–3118.
- [23] E.A. Anumol, P. Kundu, P.A. Deshpande, G. Madras, N. Ravishanker, ACS Nano 5 (2011) 8049–8061.
- [24] J. Zeng, J. Yang, J. Lee, W. Zhou, J. Phys. Chem. B 110 (2006) 24606–24611.
- [25] D.L. Huber, Small 1 (2005) 482–501.
- [26] J. Luo, L. Wang, D. Mott, P.N. Njoki, Y. Lin, T. He, Z. Xu, B.N. Wanjana, I.L.S. Lim, C. Zhong, Adv. Mater. 20 (2008) 4342–4347.
- [27] H. Tong, H. Li, X. Zhang, Carbon 45 (2007) 2424–2432.
- [28] X. Li, W. Chen, J. Zhao, W. Xing, Z. Xu, Carbon 43 (2005) 2168–2174.
- [29] Y. Wang, N. Toshima, J. Phys. Chem. B 101 (1997) 5301–5306.
- [30] Y. Liu, J. Chen, W. Zhang, Z. Ma, G.F. Swiegers, C.O. Too, G.G. Wallace, Chem. Mater. 20 (2008) 2603–2605.
- [31] B. Lim, X. Lu, M. Jiang, P.H.C. Camargo, E.C. Cho, E.P. Lee, Y. Xia, Nano Lett. 8 (2008) 4043–4047.
- [32] Z. Chen, M. Waje, W. Li, Y. Yan, Angew. Chem. Int. Ed. 46 (2007) 4060–4063.
- [33] C.H. Yen, K. Shimizu, Y. Lin, F. Bailey, I.F. Cheng, C.M. Wai, Energy Fuels 21 (2007) 2268–2271.
- [34] Y. Zhao, X. Yang, J. Tian, F. Wang, L. Zhan, Int. J. Hydrogen Energy 35 (2010) 3249–3257.
- [35] S. Wei, D. Wu, X. Shang, R. Fu, Energy Fuels 23 (2009) 908–911.
- [36] R. Narayanan, M.A. El-Sayed, J. Phys. Chem. B 109 (2005) 12663–12676.
- [37] L. Zhang, D. Xia, Appl. Surf. Sci. 252 (2006) 2191–2195.
- [38] J. Huang, Z. Liu, C. He, L.M. Gan, J. Phys. Chem. B 109 (2005) 16644–16649.
- [39] J. Zeng, J.Y. Lee, J. Chen, P.K. Shen, S. Song, Fuel Cells 7 (2007) 285–290.
- [40] N. Kristian, X. Wang, Electrochem. Commun. 10 (2008) 12–15.
- [41] X. Li, X. Qiu, H. Yuan, L. Chen, W. Zhu, J. Power Sources 184 (2008) 353–360.
- [42] A. Kabbabi, R. Faure, R. Durand, B. Beden, F. Hahn, J.M. Leger, C. Lamy, J. Electroanal. Chem. 444 (1998) 41–53.
- [43] J.H. Jiang, A. Kucernak, J. Electroanal. Chem. 543 (2003) 187–199.
- [44] C. Hsieh, J.Y. Lin, J. Power Sources 188 (2009) 347–352.
- [45] J. Jiang, A. Kucernak, J. Electroanal. Chem. 520 (2002) 64–70.
- [46] M. Gallo, Transport Policy 18 (2011) 413–424.
- [47] E. Morallón, A. Rodes, J.L. Vázquez, J.M. Pérez, J. Electroanal. Chem. 391 (1995) 149–157.
- [48] M. Watanabe, S. Motoo, J. Electroanal. Chem. 60 (1975) 267–273.
- [49] H.A. Gasteiger, N. Marković, P.N. Ross Jr., E.J. Cairns, Electrochim. Acta 39 (1994) 1825–1832.
- [50] Y. Tong, H.S. Kim, P.K. Babu, P. Waszczuk, A. Wieckowski, E. Oldfield, J. Am. Chem. Soc. 124 (2001) 468–473.